Manchester Metropolitan University

e-space
Manchester Metropolitan University's Research Repository

Please cite the Published Version

De Chowdhury, Swapnadip, Zhou, Jian Guo, Khait, Anatoliy, Pullen, Tim, Causon, Derek, Qian, Ling and Mingham, Clive (2023) Wind effects on wave overtopping at a vertical sea defence. Journal of Waterway, Port, Coastal and Ocean Engineering, 149 (4). ISSN 0733-950X

DOI: https://doi.org/10.1061/JWPED5.WWENG-1960

Publisher: American Society of Civil Engineers

Version: Accepted Version

Downloaded from: https://e-space.mmu.ac.uk/631596/

Additional Information: This material may be downloaded for personal use only. Any other use requires prior permission of the American Society of Civil Engineers. This material may be found at https://doi.org/10.1061/JWPED5.WWENG-1960

Data Access Statement: All data, models, or code that support the findings of this study are available from the corresponding author upon reasonable request.

Enquiries:
If you have questions about this document, contact openresearch@mmu.ac.uk. Please include the URL of the record in e-space. If you believe that your, or a third party's rights have been compromised through this document please see our Take Down policy (available from https://www.mmu.ac.uk/library/using-the-library/policies-and-guidelines)

Wind effects on wave overtopping at a vertical sea defence

Swapnadip De Chowdhury[1*], Jian Guo Zhou[2], Anatoliy Khait[3], Tim Pullen[4], Derek Causon[5], Ling Qian[6], and Clive Mingham[7]

[1*]Corresponding Author, Department of Ocean Engineering and Naval Architecture, IIT Kharagpur, Kharagpur, West Bengal 721302, India. Email: dcswapnadip@gmail.com

[2]Centre for Mathematical Modelling and Flow Analysis, Department of Computing & Mathematics, Manchester Metropolitan University, Manchester, M1 5GD, UK. Email: J.Zhou@mmu.ac.uk

[3]Department of Mechanical Engineering and Mechatronics, Faculty of Engineering, Ariel University, Ariel 40700, Israel. Email: haitanatoliy@gmail.com

[4]HR Wallingford, Wallingford OX10 8BA, UK. Email: t.pullen@hrwallingford.com

[5]Centre for Mathematical Modelling and Flow Analysis, Department of Computing & Mathematics, Manchester Metropolitan University, Manchester, M1 5GD, UK. Email: d.m.causon@mmu.ac.uk

[6]Centre for Mathematical Modelling and Flow Analysis, Department of Computing & Mathematics, Manchester Metropolitan University, Manchester, M1 5GD, UK. Email: l.qian@mmu.ac.uk

[7]Centre for Mathematical Modelling and Flow Analysis, Department of Computing & Mathematics, Manchester Metropolitan University, Manchester, M1 5GD, UK. Email: c.mingham@mmu.ac.uk

ABSTRACT

The wind effect on the efficiency of the coastal defence structure is studied in this paper. It is normally assumed that the strength of the wind impact is characterized by the impulse parameter.

If it is lower than a certain value, the wind is expected to have a dominant effect on the wave overtopping rate. Contrary to the regular observation, this study reports a new regime of wave overshoot when low value of the impulse parameter does not lead to importance of wind. It is argued that the new regime appears due to the triplet instability previously studied by others. The variation of the standing wave height and the overshooting jet between the sequential cycles results in independence of the overtopping rates of the wind speed.

INTRODUCTION

Many coastal structures are vulnerable to wind at moderate to high speeds during normal weather as well as a storm surge. Coastal defences are standard choices to protect the coasts against flooding from wave overtopping and yet still it is not usual to design them based on studies specifically focused on an understanding of wind effects. The primary reason is that the incorporation of a wind generation facility into an existing physical flume is not straightforward. (De Waal et al. 1996) and (Wolters and van Gent 2007) used paddle wheels rotated at a given speed to transport water spray generated due to the wave impact on the vertical structure. The wheel speed was calibrated to have enough time for the impinging water on the structure to rise up and then stick to the wheel blade. Under the assumption that all the spray that is generated due to wave impact is blown onshore by the wind, these tests aimed to account for the wind effects on overtopping in physical model tests. The tests suggested a high increase in overtopping rates by wind compared to no wind conditions in some specific types of wave impacts, although results could not be quantified fully due to the lack of proper scaling laws. (González-Escrivá et al. 2004) reproduced a real storm surge event in a laboratory and reported a significant increase in overtopping rates due to wind especially for small overtopping rates. The wind effects on overtopping (De Rouck et al. 2005) can be predicted using estimates from neural network models (van Gent et al. 2007) based on a large database created from numerous physical model tests. This can give certain factors to scale the overtopping rates without wind to account for wind effects. However, sometimes it is hard to find a physical explanation behind this scaling. As there are no reliable empirical relations for evaluating wind effects on wave overtopping, coastal engineers are left with prescribing a wide margin in the design of a coastal defence such as height. This appears to be a normal choice for places with high onshore wind speeds in particular, but clearly less economical in practice. Although much effort has been spent on understanding the wave structure interactions in overtopping under typical ambient condition with no wind speed, clearly our knowledge about wind effects on overtopping is far from being fully developed.

The studies on wind-wave interactions, see e.g. (Miles 1957), (Kharif et al. 2008), (Chalikov 1978), (Yan and Ma 2010), (Xie 2014), (Hasan et al. 2018), allow us to understand various mechanisms of energy and momentum transfer that take place, which may also be applicable to the cases of overtopping with large wind speeds. A two-phase model was also developed by (Hieu et al. 2014) and (Li and He 2011) to study wind-wave interaction at the sea wall in two dimension under relatively small wind speeds. There are several mechanisms in which wind contributes to overtopping: (1) wind energy transfer to the waves in between successive run-ups; (2) curvature of the overshooting water due to the strong shear force from the wind after wave impact and (3) wind driven surface currents in shallow waters. Mechanism (1) is mostly found in the case of a mildly sloped or curved structure, whereas, for a vertical seawall causing strong reflection of the incident waves, mechanism (2) is dominant. (Ward et al. 1996) and (Ward et al. 1998) focused on mechanism (1), where in some cases wind effects on run up and overtopping on slopes are clearly visible, especially at high wind speeds. Mechanism (2) by its nature leads to more violent wave structure interactions than the others and was considered by (De Waal et al. 1996) and (Wolters and van Gent 2007). During an extreme storm surge event mechanism (2) is encountered frequently. The waves impinging on the vertical structure may lead to high overshooting jets which can indeed increase the overtopping even at low wind speeds.

In this paper, we try to improve our current understanding on this last type of wave interactions (mechanism 2) by conducting new physical model tests and complimentary Computational Fluid Dynamics (CFD) simulations to provide conclusive support for the data from the tests. Firstly we describe the set up and the incident wave conditions for the physical model tests. We then discuss sample data from some of these tests and show the variation in the wind effects on wave overtopping subjected to change in the incident wave condition, namely the wave height and the impulse parameter. It may be noted that the height of the overshooting jet during overtopping and thus the type of interaction, i.e., violent or mild can be estimated through the impulse parameter (Van der Meer et al. 2018). Thus this is a key parameter for choosing input wave condition. More details are provided in the following.

EXPERIMENTS IN A PHYSICAL WAVE FLUME

The experiments were conducted in a shallow water wave flume at the Froude hydrodynamics laboratory at HR Wallingford, UK. The overall set up were reported previously (De Chowdhury et al. 2019; De Chowdhury et al. 2020), yet we provide details for the sake of completeness. The wave flume is 40 m length and 1.2 m wide with water depth up to 1 m. The flume is operated by a piston type wavemaker. Schematic of the flume in model scale is shown in Fig 1(a). In tests, broadband irregular waves were generated using JONSWAP spectrum formula with $\gamma = 3.3$ and used as input to obtain statistically significant results for the estimated overtopping rates. Several wave gauges were used to track the wave field during the runs. Readings from Gauge 1 recorded the time history of actual wave input by the motion of the wavemaker. Whereas, the readings from gauges 2 to 6 were used to reconstruct the incident wave conditions on the sea defence model for the purpose of numerical modelling later. More specifically, the readings from gauges 2 to 6 were utilized to separate the incident wave spectrum ($S_{\mathrm{Inc}}(f)$) from reflected spectrum ($S_{\mathrm{Ref}}(f)$) using the method by (Isaacson 1991).

Sample incident spectrum derived from one of these runs (e.g., WC09 as referred in Table 1 while discussing the details of the input waves in subsection 2) is compared with the target JONSWAP spectrum in Fig 2. The measured spectrum is not as narrow banded as the target spectrum and rather significantly spread over the higher frequencies. The region of measurements is characterized by wave breaking due to violent interaction with the sea defence and includes reflected waves from the model seawall. Thus the measured spectrum is not exactly similar to the target spectrum in this case and the significant wave height in the measured spectrum is higher by 14% as it contains reflected wave components. This indicates some shortcoming of the method adopted to segregate the incident waves purely from the reflected waves in such fairly complex wave environment. Using this measured incident wave spectrum $S_{\mathrm{Inc}}(f)$ directly as input to the numerical model allows us to efficiently replicate the wave environment observed during the physical tests.

The wavemaker was run with the active wave absorption in order to effectively absorb the reflected waves. We fabricated a sea defence model replicating the Livermeade profile at a scale $1 : 17$ of model to prototype. The window as shown in the schematic in Fig 1, facilitated visualizations of the wave interactions with the sea defence model during several overtopping cycles.

Several non-connected compartments (as shown in Fig 1(b)) were installed after the sea defence model to collect and measure the amount of the overtopping water. The dip sticks were used to measure increase in the water levels inside these compartments during the tests. Excess of water were duly extracted using pumps. Measurements from these dip sticks and the record of the volume of the water that were pumped out together lead to estimates of the distributions of the overtopping rates as function of the distance onshore from the sea defence model. We used two rows of fans (each with two fans) in front of the sea defence model to mimic a wind field for the test cases with a given wind speed. The power input to the fans were controlled through the wind dial gauges.

It is important to note that before arriving at the sea defence the incident wave is already affected by the wind field in an actual coast. The overtopping due to incident wave which already interacted with a wind will be different from that due to wave which itself is not affected by wind. However, this requires studying wind wave interactions at long fetch, which is a different problem from what we study in this paper, i.e., investigating wind effects on the overtopping waves.

Input wave conditions and the impulse parameter

We used a range of irregular wave conditions as input (as shown in Table 1 in prototype scale) in order to obtain a realistic sea state that the sea defence prototype may be subjected to. Each of the test runs were repeated two times to gain some confidence levels on the measured data. Moreover, each test run had three subsets and was subjected to identical input wave conditions: one with no wind speed; other with wind speed dial 7 referring to wind speed 1.4 m/s and still other with wind speed dial 10 referring to wind speed 1.7 m/s. These wind speeds were actually measured at the crest of the sea defence using digital anemometer which can be hand-held at a desired location.

Our choice for the various input wave conditions is primarily based on the impulse parameter $\mathcal{I}$ which is given by (Van der Meer et al. 2018) as

$$\mathcal{I} = \frac{h^2}{H^{\mathrm{p}}_{m0}\lambda_{m-1,0}}, \tag{1}$$

where h is the initial water depth at the toe of the sea defence; H^{p}_{m0} is the spectral wave height in prototype scale, i.e. the significant wave height (Van der Meer et al. 2018) and $\lambda_{m-1,0}$ is the characteristic deep water wave length, i.e, $\lambda_{m-1,0} = \mathrm{g}T^2_{m-1,0}/(2\pi)$ and $T_{m-1,0}$ is $1.1T^{\mathrm{p}}_p$ where T^{p}_p is the peak wave period in prototype scale. The studies (e.g., (Van der Meer et al. 2018)) show that when $\mathcal{I} \leq 0.23$, the wave interaction with the sea defence leads to a high overshoot and the probability of significant wind effect on overtopping increases. The overshooting jet due to a impulse type wave interaction greatly depends on the stability of the standing wave field at the vertical sea defence.

Energy of standing wave

It is useful to plot the energy of the standing waves at the sea defence model owing to various input wave conditions (i.e., from Table 1) as a function of wave steepness ka, see Fig. 3, where k is the wave number and a is the amplitude of the waves. It is worthwhile to mention that here we use the measurements from the wave gauges adjacent the sea defence model to construct the total (i.e., combined incident and reflected) wave energy spectrum. The significant wave height (H^{m}_{m0}) in model scale due to the combination of incident and reflected waves is related to the respective spectrum as $H^{\mathrm{m}}_{m0} = H_{\mathrm{Inc}} + H_{\mathrm{Ref}}$ where H_{Inc} is the significant wave height in the incident spectra and H_{Ref} is the significant wave height in the reflected spectra. These wave heights are obtained from the respective spectra as $H_{\mathrm{Inc}} = 4\sqrt{m_{0,\mathrm{Inc}}}$ and $H_{\mathrm{Ref}} = 4\sqrt{m_{0,\mathrm{Ref}}}$ with

$$m_{0,\mathrm{Inc}} = \int_0^\infty S^2_{\mathrm{Inc}}(f)\,\mathrm{d}f \quad \text{and} \quad m_{0,\mathrm{Ref}} = \int_0^\infty S^2_{\mathrm{Ref}}(f)\,\mathrm{d}f, \tag{2}$$

and then it is straightforward to obtain wave amplitude a from H^{m}_{m0}. The wave period in model scale, i.e., T^{m}_{p} is the peak wave period we can identify from the incident spectra $S_{\mathrm{Inc}}(f)$. The wave number k is obtained from linear wave dispersion using this peak wave period and local water depth h in model scale. The energy of the linear wave is $E = \rho g \left(H^{\mathrm{m}}_{m0}\right)^2/8$, as discussed in Appendix I.

According to the physical model tests by (Longuet-Higgins and Drazen 2002) on steep waves interacting with a vertical wall, when the steepness ka of the incident wave is in the range of $0.285 \leq ka \leq 0.443$, the resulting standing wave at a fully impermeable vertical structure is unstable, often leading to triplets where each of the third wave is the highest among three consecutive wave cycles impinging on the structure. This critical range is shown by the two vertical lines in Fig. 3. All our test cases considered in the physical model were within this critical range and thus we were supposed to observe a variety in the heights of the overshooting jets. However, the range of the impulse parameter was wide $0.02 \leq \mathcal{I} \leq 0.05$ suggesting that in some cases the interactions were presumed to be mild, i.e. when $\mathcal{I} > 0.023$.

As one can see, the linear theory suggests that the energy of the standing wave grows quadratically; whereas the nonlinear theory (i.e., the second order theory based on (Chen et al. 1988)) conforms to an upper limit. The energy estimates from the nonlinear standing wave theory are found to be much closer to the physical model tests. The energy predicted by the nonlinear theory is always less than that by linear theory over the range of the wave steepness. We provide some explanation behind this phenomena in the Appendix I.

RESULTS FROM LABORATORY EXPERIMENTS

The overtopping rates with and without wind action for the various incident wave conditions as listed in Table 1 were the primary aims of the measurements. The prefix 'WC' refers to various wave conditions, whereas the suffix 'wsd' refers to different wind speed dials. We can group the wind affected overtopping due to various incident wave conditions into three large types as described below. The grouping is aimed at categorizing three types, i.e., small wind effect; negative wind effect where there is a decrease in overtopping rates in the presence of a given wind speed; and significant wind effect.

Type A

The spectral wave heights and impulse parameters for these cases were within $2.44 < H^{\mathrm{p}}_{m0} < 2.8$m and $0.02 < \mathcal{I} < 0.04$. The peak periods were close to 11 s. The variation in the overtopping rates measured over the distance d_{sc} from the sea defence model is shown in Fig. 4. For this type of overtopping, we can clearly see that the effects of the wind speeds is quite negligible immediately after the sea defence, see wsd7 and wsd10 referring to wind speed dials 7 and 10, i.e. 1.4 m/s and 1.7 m/s, respectively. At some distance (around 5 m), an increase in the overtopping rates was observed as a result of wind speeds corresponding to wave condition WC03. On the contrary, for wave condition WC010, the effect of wind with the speed wsd7 is hardly distinguishable from that of ws0. Only for for wsd10 there is an increase in the overtopping rates around 5m from the sea defence.

Type B

Wave conditions in these type also had similar variations in the spectral wave heights and impulse parameters as in Type A but relatively smaller peak periods, close to 10 s. As shown in Fig. 5, this type is characterised by reduction in overtopping rates in presence of wind. Such an effect is the most drastic in the case of wave condition WC04. However, the increase in the overtopping rates without wind action is followed by its reduction at larger distances (around 4 m) from the defence. The overshooting jet disintegrates into small water fragments during recession of the jet under the action of gravity after the initial impact. Most of the water falls on the tank immediately after the sea defence. These small fragments are easily carried away by the wind drag if it is present. This explains the reduction in the overtopping rates immediately after the sea defence for WC04 when the wind is in action.

For the other two conditions, i.e. WC08 and WC11, the overtopping rates are consistently lower in the presence of wind throughout the distances. In this regard, it is important to refer to the impulse parameter $\mathcal{I}$ in between these wave conditions. The parameter $\mathcal{I} = 0.022$ for WC04, whereas $\mathcal{I} > 0.04$ for WC08 and WC11. Therefore, WC04 is characterized by strongest impulse type interaction. This makes the overtopping process in WC04 quite different, even though the significant wave height H^{p}_{m0} is little lower as compared to WC08 and WC11 (see Table 1). From engineering point of view, information about this type of overtopping under WC04 may be very useful, since in practice many of the existing transport links are located close to the coastal defence system. Thus they are exposed to higher hazard even with small to moderate wind speeds during overtopping.

Type C

Wave conditions for this type had smaller peak periods compared to other two types, i.e. nearly 9.7 s. For this type of overtopping, the wind effects are found to enhance the overtopping rates for all of the wave conditions as shown in Fig 6. Specifically, for WC07, the wind action resulted in overtopping rates two times higher as compared to that without wind near the sea defence. For WC09, the overtopping rates increase gradually with wind speed across all the distances from the sea defence.

NUMERICAL SIMULATIONS OF WIND INDUCED OVERTOPPING

While laboratory experiments allowed us to observe a variety of overtopping types under the effect of wind, we still do not understand well the physical reasons behind it. To get a better insight into the wave structure interaction process we performed a series of numerical simulations in 2D domain. The numerical model we used is based on the open-source computational fluid dynamics (CFD) library OpenFOAM® based on finite volume method. The appearing two-phase flow (water and air) is resolved by the volume-of-fluid (VoF) method with additional free surface compression to keep the interface sharp. We also used the open-source library olaFlow (Higuera et al. 2013) to obtain proper boundary conditions at the inlet for wave generation. Active wave absorption was used at the inlet to achieve steady overtopping cycles. The second-order schemes were used in finite volume method to discretize the spatial terms of the flow governing equations, while the time marching was done using the standard first-order Eulerian scheme. Within the structure of OpenFOAM, the framework named `‘fvOptions’` allows defining an external force mimicking a wind field to be imposed on the main solver, without modifying the in-built PISO implementations. The desired region with a given wind speed can be defined as a `cellZone` and referred details like the input wind speed, duration of the wind activity. In this way we were able to induce the air motion near the sea defence through the additional source term in the Reynolds Averaged Navier-Stokes (RANS) equations. This is same as what we adopted in (De Chowdhury et al. 2021). This wind generation is duly validated in our previous works, i.e, in (De Chowdhury et al. 2019) and in the appendix to (De Chowdhury et al. 2021). All the simulations are performed using the OpenFOAM ESI version 1706.

The computational domain comprised of a constant water depth region from the location of wave gauge 2 (as seen in Fig. 1) to the sea defence model. The mesh structure near the sea defence model is shown in Fig. 7. From inlet to the sea defence model, there are 315 cells along the x-axis; 90 cells along the z-axis and 1 cell along the y-axis. We gradually compressed the mesh along z-direction. The non-uniform regions in the top (20% of z-direction) and in the bottom (10% of z-direction) both has an expansion ratio of 1:8 and together consists of 30% of the number of cells. The remaining 70% of the cells are distributed uniformly in the remaining 70% portion along z-direction. Additionally, the mesh was refined in two levels (the first level has cell width which is half of that of background mesh and the second level has cell width which is one fourth of that of background mesh) along x-direction to best capture the free surface dynamics on the sea defence model. The background mesh is selected based on convergence of wave elevation time history adjacent to the inlet. The convergence of the free surface elevation measured at 1.2m from the inlet for WC09 (incident wave spectrum as shown in Fig. 2) is evidenced by Fig. 8. Here, mesh 1 is the background mesh described above; mesh 2 is of background mesh with number cells that is 1.5 times of that of mesh 1 along x-axis and mesh 3 is the same with number cells that is 2 times that is of mesh 1 along x-axis. All three meshes have same aspect ratio. Furthermore, a sample wave elevation time history measured at the same location using mesh 1 but without active wave absorption is also depicted in Fig. 8 upto the same time duration. This clearly shows the efficiency of the active wave absorption available in olaFlow in maintaining the desired mean water level. We refer the readers to (Higuera et al. 2013) and (Miquel et al. 2018) for extensive validations of this active wave absorption. Success of the numerical wave making with mesh 1 is depicted in

Fig. 9 which clearly shows that the numerical solver properly captures the highly nonlinear wave propagation as indicated by the chosen input spectrum WC09 in section 2.

The wind region on the sea defence is outlined in red in Fig. 7. The geometrical configuration of this zone is selected based on multiple runs with varying sizes. The RANS closure based on the reliable $k - \omega$ SST turbulence model as discussed in (Devolder et al. 2018) was applied. The turbulence generated during the wave breaking on the sea defence was accounted by the turbulence model modifications implemented in olaFlow library.

In the physical model tests the irregular waves impact covered around 1000 wave cycles. It would be highly computationally expensive to replicate such test in the CFD model to quantify the subtle differences in the overtopping behaviours with and without wind action. Note that the impulse parameter which controls the wave impact depends on the characteristic spectral wave height and deep water wave length. Therefore, it might be possible to simulate the dominant wave interaction process by using a regular wave field with the given parameters as input in the model. More specifically, the regular wave field is defined with a wave height same as H^{m}_{m0}, i.e., the significant wave height and a peak wave period both in model scale. This is same as what we adopt to find the wave steepness and energy as described in Subsection 2. The wave heights H^{m}_{m0} and wave periods T^{m}_{p} used in the numerical simulations for three different cases are provided in Table 2. This allows qualitative analysis and discussion of the overtopping we observed in the physical model tests.

We choose WC03, WC04 and WC09 representative of Type A, Type B and Type C to investigate the overtopping in more detail in the following. The wind flow of the prescribed speeds varied greatly in these types and the numerical simulations gave us the scope to track those details, which otherwise were not available from the measurements in the physical model tests. Moreover, both the physical model tests (see section 3) and the numerical simulations were conducted in the model scales. The wind speeds remained unchanged in both models since it could not be Froude scaled.

WC03, Type A

The overshooting wave profiles during the wave impact on the sea defence is shown in Fig. 10(a) and Fig. 10(b). The wave interaction is characterised by a very high overshoot owing the impulse parameter is low in this case. A continuous thick overshooting jet observed without wind. But this is disintegrated into smaller fragments in the presence of the wind speed. However, these smaller fragments are not significantly affected by the wind speed variation. It could be explained by the strong velocity gradient offshore due to the violent breaking wave impact on the sea defence, see Fig. 10(c) and Fig. 10(d). The velocity field induced in the air by the wave in absence of wind is found to be of similar strength of that prescribed by wind velocity, i.e. nearly 1.55 m/s, i.e., Fig. 10(e) and Fig. 10(f). This suggests that apart from more fragmentation, the wind action does not contribute appreciably in the overtopping. Under their own weight, the fragmented water falls back into the same tanks they would fall under no wind action.

WC04, Type B

Flow field evolution in one of the overtopping cycles is shown in Fig. 11. The high overshooting jet still occurs, cf. Fig. 11(a) and Fig. 11(b). However, the velocity field in the air phase under no wind action is quite different from that we see in Type A above. The air velocity field is focused on the sea defence crest when there is no wind imposed externally, see Fig. 11(c) and Fig. 11(d). Under the action of the prescribed wind speed, i.e. Fig. 11(c) and Fig. 11(d), this high velocity region is diffused on much larger area beyond the sea defence. This causes a significant reduction in the available wind induced lift that holds the water jet upright. This is evident from the comparison of the free surface profiles in Fig. 11(a) and Fig. 11(b) given for the no wind and wind induced cases. If the air flow is induced by the wind, much of water which would otherwise fall into the container immediately after the sea defence, now falls back into the wave tank in front of the sea defence.

WC09, Type C

Similar to Type B, the wave interaction in Type C is also characterized by a focused high velocity region in the air phase, see Fig. 12(c). However, the size of this zone is much smaller in the case of Type C mainly because the impulse parameter is the highest (i.e. 0.046 as seen from Table 1).

This means that the wave interaction is less violent compared to Type A and Type B. As a result, the overshooting jet (Fig. 12(a)) is much thinner in contrast with other two cases.

Next, while we consider the wind speeds in the numerical simulations for type C, we can clearly observe two distinct velocity zones in the air phase in both Fig. 12(e) and Fig. 12(f). At the sea defence crest the velocity field is discontinuous, while a bit above it there is a continuous high velocity region. This creates an adverse pressure gradient acting downwards and preventing the water jet to go upward in the presence of the wind-induced airflow. This is clearly seen from the free surface profiles captured in Fig. 12(a). Part of the water jet which goes above freely under its own momentum (with no wind) can fall into the more distant container. However, the wind-induced adverse pressure gradient forces the water to fall only into the tank immediately after the sea defence as seen in Fig. 12(b). Thus the primary reason of increasing overtopping rates in Type C is an adverse pressure gradient field induced by the imposed wind speed.

IMPACT OF THE SEA DEFENCE BOARD ON THE OVERTOPPING RATES

The non-dimensional overtopping rates as measured in the physical model tests are plotted in Fig. 13 as a function of the sea defence board height (R_c), significant wave height (H_{m0}^{p}) and wave steepness ka. The variation of the wave steepness is shown as different types of lines which are polynomial fit of the order 2 through the data. The sea defence board height is defined as the elevation of the sea defence crest above the initial calm water level. The normalization of R_c with respect to the spectral wave height H_{m0}^{p} is introduced. The effect of the two wind speeds corresponding to dials wsd7 and wsd10 (1.4m/s and 1.7m/s, respectively) is non-uniform over the range of R_c/H_{m0}^{p} under investigation. At high R_c/H_{m0}^{p} corresponding to small relative incident spectral wave height (and high wave steepness), the wave interaction with the sea defence is mild and the wind effects are minimal. The wind effects are most dominant in the range $1.9 < R_c/H_{m0}^{\mathrm{p}} < 2.4$. For instance, for $R_c/H_{m0}^{\mathrm{p}} = 1.95$, there is almost 40% increase in the overtopping rates due to wsd10 as compared to wsd0. If the impulse parameter was the sole criteria for indicating the wind effects, we would have found a very similar wind impact at smaller R_c/H_{m0}^{p} as well.

However, at low value of R_c/H_{m0}^{p} (when wave steepness is moderate) when the spectral wave height is significant, the wave interaction is extremely violent, which is inconsistent with the impulse parameter criteria. In the case of small R_c/H^{p}_{m0} the impulse parameter is $\mathcal{I} < 0.023$, suggesting that the wind effect should be strong. Nevertheless, the differences in the overtopping rates with and without wind are hardly distinguishable. Such an inconsistency in the overtopping behaviour can be explained using the nonlinearity that we see in the standing wave energy in Fig. 3. For instance, numerical simulations of Type A and Type B above corresponding to wind conditions WC03 and WC04 are much closer to the lower limit of the critical wave steepness (i.e. 0.285). On the contrary, wind condition WC09 for Type C is much closer to the upper limit which means it is more unstable compared to others. The appearance of triplet instability (Longuet-Higgins and Drazen 2002) leads to a greater variety in size and shapes of the overshooting jets contrary to what we observe in stable overtopping cycles.

CONCLUSIONS

In this paper we report a set of results of wind effects measured recently on the scaled model of the sea defence in a physical wave flume. Much of the wind effects depend directly on the thickness of the overshooting jet. It was found that the impulse parameter $\mathcal{I} < 0.023$ leads to a impulse type interaction of the wave with the sea defence and thus high overshoot in general. Such parameterization works well only for relatively low waves with low steepness. In these cases, a significant wind speed was found to result in the maximum increase in the overtopping rate nearly 1.5.

A certain regime was observed where the overtopping rate is independent of the wind speed despite the low value of the impulse parameter $\mathcal{I} < 0.023$. Such non-trivial effect was attributed to high nonlinearrity of the incident wave. If the incident wave steepness (defined by peak wave period and spectral wave height) is high and within the critical range, the standing wave energy starts to plays a vital role in determining the shape of the overshooting jet. Furthermore, such an effect is slightly pronounced even at relatively low wave steepness close to 0.285. For example, for WC03 the shape of overshooting jet is thin (Fig. 10(b)) but the wind effect is still small.

To gain a physical understanding of such an observation we have performed a series of numerical simulations accounting for the wind effects similar to those in the laboratory model tests. A variety of velocity fields in the air phase were obtained, which helped us to explain the different types of overtopping behaviour. While the impulse parameter is close to 0.23 and still slightly less than that, if the incident wave steepness is near the lower limit of the critical regime, the velocity field in the air phase induced by the tripplet instability (originally found by (Longuet-Higgins and Drazen 2002)) is unaltered by a moderate wind speed. This leads to a new regime (evidenced through overtopping Type A in this paper) of wave-structure interactions when the overtopping rates are independent of the wind speed. All three types of overtopping (Types B and C for negative and positive wind effect, respectively) are denoted in Table 1 for easy reference.

It can be also reported that the interaction of thick overshooting jets with high wind speed may lead to more fluctuations in the distribution of overtopping rates across the distance from the sea defence onshore. Thus it is an important topic to study in future to gain more comprehensive insights of the overall wind effects on the wave overtopping.

APPENDIX I. ON THE ENERGY OF NONLINEAR STANDING WAVE

The observations used in the course of the study show that the energy of nonlinear standing wave is always lower as compared to the regular linear wave of the same crest-trough height H, see Fig. 3. This observation is not necessarily trivial from the physical point of view and requires consideration.

Following (Chen et al. 1988), we assume the potential flow with the velocity field

$$\{u, w\} = \left\{\frac{\partial \phi}{\partial x}, \frac{\partial \phi}{\partial z}\right\} \tag{3}$$

governed by the Laplace equation leading to the solution in the following form:

$$\phi(x, z, t) = C_1 \frac{\cosh(k(h+z))}{\cosh(kh)} \cos(kx) \sin(\omega t), \tag{4}$$

where C_1 is the amplitude constant. The function ϕ should satisfy nonlinear kinematic and dynamic free surface boundary conditions:

$$\begin{aligned} & g\eta + \frac{\partial \phi}{\partial t} + \frac{1}{2}\left[\left(\frac{\partial \phi}{\partial x}\right)^2 + \left(\frac{\partial \phi}{\partial z}\right)^2\right] = 0 \\ & \frac{\partial \eta}{\partial t} - \left(\frac{\partial \phi}{\partial z} - \frac{\partial \phi}{\partial x}\frac{\partial \eta}{\partial x}\right) = 0 \end{aligned} \tag{5}$$

Combining boundary conditions together leads to the expression for the surface elevation η. Further substitution of (4) yields:

$$\begin{aligned} \eta(x,t) = & -\frac{C_1 \omega}{g} \frac{\cosh(kh + k\eta(x,t))}{\cosh(kh)} \cos(kx)\cos(\omega t) \\ & -\frac{C_1^2 k^2}{8g}\left(\frac{\cosh(2kh + 2k\eta(x,t)) - \cos(2kx)}{\cosh(kh)^2}\right)(1 - \cos(2\omega t)) \end{aligned} \tag{6}$$

Assuming further $t = 0$, it is seen that the maximum of η (designated η_0) in (6) appears at $x = 0$, while its minimum η_π is at $kx = \pi$. The crest-trough wave height for nonlinear wave is $H = \eta_0 - \eta_\pi$.

Applying (6) leads to the expression for the amplitude constant C_1:

$$C_1 = \frac{gH\cosh(kh)}{\omega\left(\cosh(kh + k\eta_0) + \cosh(kh - kH + k\eta_0)\right)}, \tag{7}$$

where $\eta_0 = \eta(x = 0, t = 0)$. Numerical solution of the recurrent equations (6) and (7) produces the approximate shape of the nonlinear standing wave in agreement with (Chen et al. 1988). Note that neglecting the $O(C_1^2)$ term and assuming $\eta = 0$ on the right-hand-side of (6) restores the solution for the linear wave of the height H and $C_1 = -gH/(2\omega)$ in agreement with (7):

$$\eta = \frac{H}{2}\cos(kx) \tag{8}$$

Normalized plot of the free surface shape for the monochromatic deep water wave is presented in Fig. 14. The linear wave corresponds to the steepness $\epsilon \to 0$, while limiting steepness was assumed according to the Stokes theory as $\epsilon \approx 0.444$. Note the difference between the linear and nonlinear wave shapes. Namely, the wave height H is composed of only 1st-order terms in the case of linear wave, where as it is split between 1st-order and higher-order terms in the case on nonlinear wave. Taking into account that 1st-order and higher-order terms contribute differently into the total wave energy, it is expected that nonlinear wave will be characterized by the energy sufficiently different from the linear approximation for the wave of the same height.

The expression for the potential and the kinetic energies (E_{vs} and E_{ks}) averaged over the wave length λ are (Dean and Dalrymple 1991):

$$\begin{aligned} E_{vs} &= \frac{1}{\lambda}\int_x^{x+\lambda} \rho g\left(\frac{(h+\eta)^2}{2} - \frac{h^2}{2}\right)\mathrm{d}x \\ E_{ks} &= \frac{1}{\lambda}\int_x^{x+\lambda}\int_{-h}^{\eta} \frac{\rho}{2}\left(u^2 + v^2\right)\mathrm{d}x\mathrm{d}z \end{aligned} \tag{9}$$

Substitution (3) and (6) to the above expressions leads to $O(C_1^2)$ nonlinearity term accounted for.

Integration of (9) yields:

$$\begin{aligned} E_{total} &= E_{vs} + E_{ks} \\ &= \frac{1}{8}\rho \mathrm{g} H^2 G^{-2} \sinh^2(kh), \end{aligned} \tag{10}$$

where

$$G = \sinh(kh + k\eta_0) + \sinh(kh + k\eta_0 - kH). \tag{11}$$

The ratio of the nonlinear wave energy (10) to the linear approximation for the wave energy is:

$$\frac{E_{nonlinear}}{E_{linear}} = \frac{\frac{1}{8}\rho \mathrm{g} H^2 G^{-2} \sinh^2(kh)}{\frac{1}{8}\rho \mathrm{g} H^2} = G^{-2}\sinh^2(kh) < 1 \tag{12}$$

It can be shown that in both deep and shallow water the energy ratio above is always below unity. This shows that the energy of nonlinear wave is always below the linear approximation of that energy for the same wave height.

APPENDIX II. NOTATION

The following symbols are used in this paper:

$\mathcal{I}$	=	impulse parameter;
h	=	initial water depth at the toe of sea defence (m);
H	=	generic regular wave height (m);
H_{m0}^{p}	=	spectral wave height in protype scale (m);
T_p^{p}	=	peak wave period in prototype scale (s);
T_p^{m}	=	peak wave period in model scale (s);
H_{m0}^{m}	=	spectral wave height in model scale (m);
$S_{\mathrm{Inc}}(f)$	=	incident wave spectrum (m^2/Hz);
$S_{\mathrm{Ref}}(f)$	=	reflected wave spectrum (m^2/Hz);
H_{Inc}	=	significant wave height in the incident spectra;
H_{Ref}	=	significant wave height in the reflected spectra;
$m_{0,\mathrm{Inc}}$	=	zeroth moment of the incident spectra;
$m_{0,\mathrm{Ref}}$	=	zeroth moment of the reflected spectra;
f	=	wave frequency (Hz);
ω	=	angular frequency (rad/s);
$\lambda_{m-1,0}$	=	deep water wave length (m);
E	=	Standing wave energy flux (kg/s^2);
ρ	=	density of water (kg/m^3);
k	=	wave number (m^{-1});
a	=	wave amplitude (m);
R_c	=	sea defence crest free-board (m);
q	=	overtopping rates per unit width of the sea defence ($\mathrm{l}/\mathrm{s}/\mathrm{m}$);
d_{sc}	=	distance from the sea defence crest (m);
g	=	acceleration due to gravity ($9.81\mathrm{m}^2/\mathrm{s}$); and
x, y, z, t	=	spatial variables (m) and time variable (s).

Data Availability Statement

All data, models, or code that support the findings of this study are available from the corresponding author upon reasonable request.

Acknowledgments

This project was funded by NERC, UK under grant number NE/R009155/1 and CIRIA, UK to whom we are very grateful. We are grateful to E. Silva for her support during the experiments at HR Wallingford. We acknowledge National Supercomputing Mission (NSM) for providing computing resources of 'PARAM Shakti' at IIT Kharagpur, which is implemented by C-DAC and supported by the Ministry of Electronics and Information Technology (MeitY) and Department of Science and Technology (DST), Government of India. We are grateful to the Reviewers for their constructive comments.

REFERENCES

Chalikov, D. (1978). “The numerical simulation of wind-wave interaction..” Journal of Fluid Mechanics, 87, 561–582.

Chen, X. Y., Tsai, C. P., and Hwung, H. H. (1988). “The Theoretical Studies on Nonlinear Standing Waves.” *Proceedings of Nonlinear Water Waves, IUTAM Symposium*, K. Horikawa and H. Maruo, eds., Tokyo, Japan, 135–142.

De Chowdhury, S., Causon, D., Qian, L., Mingham, C., Chen, H., Lin, Z., Zhou, J. G., Pullen, T., Silva, E., Hu, K., Russel, M., Manson, S., Winter, H., Joly, A., Stewart, D., and Wood, M. (2019). “Investigation of wind effects on wave overtoppinga at sea defences.” *Proceedings of 8th Coastal Structures Conference*, N. Goseberg and T. Schlurmann, eds., Hannover, Germany, 841–850.

De Chowdhury, S., Zhou, J. G., Khait, A., Causon, D., Qian, L., Mingham, C., and Pullen, T. (2021). “Local overshoot and wind effects on wave overtopping at vertical coastal structures.” *Proceedings of the Institution of Civil Engineers - Maritime Engineering*, 176(1), 3–13.

De Chowdhury, S., Zhou, J. G., Qian, L., Causon, D., , Mingham, C., , Pullen, T., Hu, K., Russel, M., Manson, S., Stewart, D., Wood, M., Winter, H., and Joly, A. (2020). “Wind effects on wave overtopping at the vertical sea defence.” *Proceedings of the Coastal Engineering Conference*, P. Lynett, ed., Online, 1–7.

De Rouck, J., Geeraerts, J., Troch, P., Kortenhaus, A., Pullen, T., and Franco, L. (2005). “New results on scale effects for wave overtopping at coastal structures.” *Proceedings of International Conference on Coastlines, Structures and Breakwaters*, N. W. H. Allsop, ed., London, UK.

De Waal, J. P., Tönjes, P., and van deer Meer, J. (1996). “Wave overtopping of vertical structures including wind effect.” *Proceedings of 25th Coastal Engineering Conference*, B. L. Edge, ed., Orlando, Florida, USA, 2216–2229.

Dean, R. G. and Dalrymple, R. A. (1991). *Water Wave Mechanics for Engineers and Scientists*. WORLD SCIENTIFIC, <https://www.worldscientific.com/doi/abs/10.1142/1232>.

Devolder, B., Troch, P., and Rauwoens, P. (2018). “Performance of a buoyancy-modified k-ω and k-ω sst turbulence model for simulating wave breaking under regular waves using openfoam®." *Coastal Engineering*, 138, 49–65.

González-Escrivá, J. A., Garrido, J. M., Medina, J. R., and Geeraerts, J. (2004). "Laboratory real storm reproduction using wind." *Proceedings of 29th Coastal Enginering Conference*, J. M. Smith, ed., Vol. 1, Lisbon, Portugal, 677–689.

Hasan, S. A., Sriram, V., and Paneer Selvam, R. (2018). "Numerical modelling of wind-modified focused waves in a numerical wave tank." Ocean Engineering, 160, 276–300.

Hieu, P. D., Vinh, P. N., Toan, D. V., and Son, N. T. (2014). "Study of wave-wind interaction at seawall using a numerical wave channel." Applied Mathematical Modelling, 38, 5149–5159.

Higuera, P., Lara, J., and Losada, I. J. (2013). "Realistic wave generation and active wave absorption for Navier-Stokes models: Application to OpenFOAM®." Coastal Engnieering, 71, 102–118.

Isaacson, M. (1991). "Measurement of regular wave reflection." Journal of waterway, port, coastal and ocean engineering, 117(6), 553–569.

Kharif, C., Giovanangeli, J. P., Touboul, J., Grare, L., and Pelinovosky., E. (2008). "Influence of wind on extreme wave events.." Journal of Fluid Mechanics, 594, 209–247.

Li, T. and He, W. (2011). "Numerical simulation of wind effects on wave overtopping by a two-phase solver." *Proceedings of Twenty-first International Offshore and Polar Engineering Conference*, 903–909.

Longuet-Higgins, M.-S. and Drazen, A. (2002). "On steep gravity wave meeting a vertical wall: a triple instability." Journal of Fluid Mechanics, 466, 305–318.

Miles, J. (1957). "On the generation of surface waves by shear flows." Journal of Fluid Mechanics, 3, 185–204.

Miquel, A. M., Kamath, A., Alagan Chella, M., Archetti, R., and Bihs, H. (2018). "Analysis of different methods for wave generation and absorption in a cfd-based numerical wave tank." *Journal of Marine Science and Engineering*, 6(2).

Van der Meer, J., Allsop, N. W. H., Bruce, T., De Rouck, J., Kortenhaus, A., Pullen, T., Schüttrumpf, H., Troch, P., and Zanuttigh, B. (2018). EurOtop. Manual on wave overtopping of sea defences and related structures. An overtopping manual largely based on European research, but for worldwide application, <http://www.overtopping-manual.com>.

van Gent, M. R. A., Van den Boogaard, H., Pozueta, B., and Medina, J. R. (2007). "Neural network modelling of wave overtopping at coastal structures." Coastal Engineering, 54, 583–593.

Ward, D., Wibner, C. G., and Zhang, J. (1998). "Runup on coastal revetments under the influence of onshore wind." Journal of Coastal Research, 14(4), 1325–1333.

Ward, D., Zhang, J., Wibner, C. G., and Cinotto, C. M. (1996). "Wind effects on runup and overtopping of coastal structures." *Proceedings of 25th Coastal Engineering Conference*, B. L. Edge, ed., Orlando, Florida, USA, 2206–2215.

Wolters, G. and van Gent, M. R. A. (2007). "Maximum wind effect on wave overtopping of sloped coastal structures with crest elements." *Proceedings of 5th Coastal Structures Conference*, L. Franco, G. R. Tomasicchio, and A. Lamberti, eds., Venice, Italy, 1263–1274.

Xie, Z. (2014). "Numerical modelling of wind effects on breaking solitary waves." European Journal of Mechanics- B/Fluids, 43, 135–147.

Yan, S. and Ma, Q. (2010). "Numerical simulation of interaction between wind and 2D freak waves." European Journal of Mechanics- B/Fluids, 29, 18–31.

List of Tables

TABLE 1. Incident wave conditions (in prototype scale) used in the physical model tests. Here H^{p}_{m0} and T^{p}_{p} are the spectral wave height and peak wave period in prototype scale for combination of Still Water Levels (SWL), which are defined with respect to the sea bed. The corresponding impulse parameters $\mathcal{I}$ are given as well.

Incident wave condition	SWL(m)	H^{p}_{m0}(m)	T^{p}_{p}(s)	$\mathcal{I}$	wave steepness ka	overtopping type
WC03	2.31	2.44	11.0	0.021	0.33	A
WC04	2.31	2.41	10.5	0.022	0.35	B
WC05	2.31	2.46	12.0	0.017	0.31	A
WC06	3.0	2.55	9.72	0.04	0.40	C
WC07	3.0	2.66	10.0	0.038	0.39	C
WC08	3.3	2.85	10.22	0.041	0.38	B
WC09	3.3	2.66	9.57	0.046	0.45	C
WC10	3.5	2.80	9.92	0.045	0.43	A
WC11	3.5	2.89	10.07	0.043	0.41	B

Incident wave condition	H_{m0}^{m}(m)	T_p^{m}(s)
WC03	0.096	2.89
WC04	0.09	2.67
WC09	0.12	2.32

TABLE 2. Incident wave heights and periods used for regular waves as input to the numerical simulations.

List of Figures

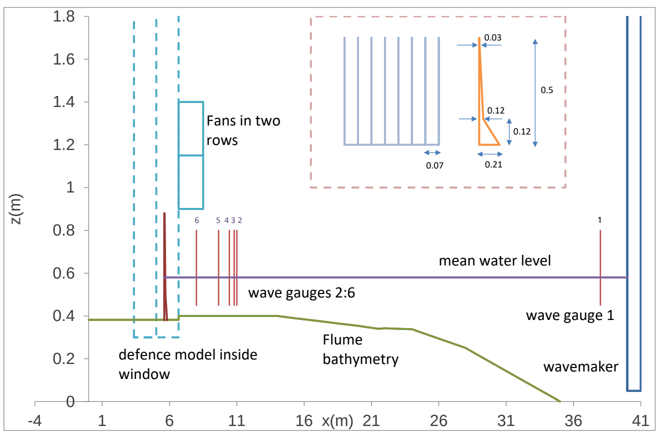

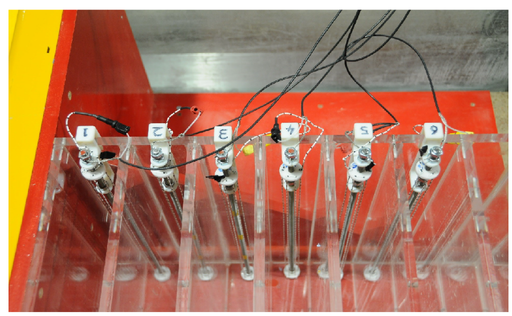

(a) **(b)**

Fig. 1. (a) Schematic of the wave flume (in model scale) in the hydrodynamics testing facility at HR Wallingford. The placement of the sea defence model in the wave flume is shown in a schematic along with the details of the sea defence and the overtopping tank model with identical compartments in the inset.(b) Picture of the overtopping tank used in the physical modelling.

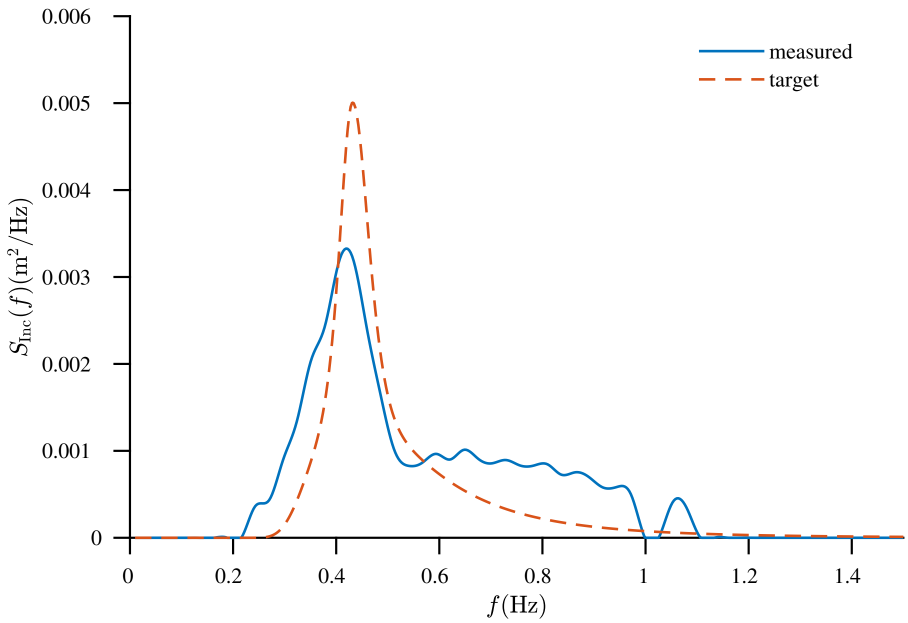

Fig. 2. Sample spectrum for WC09 used for the numerical model.

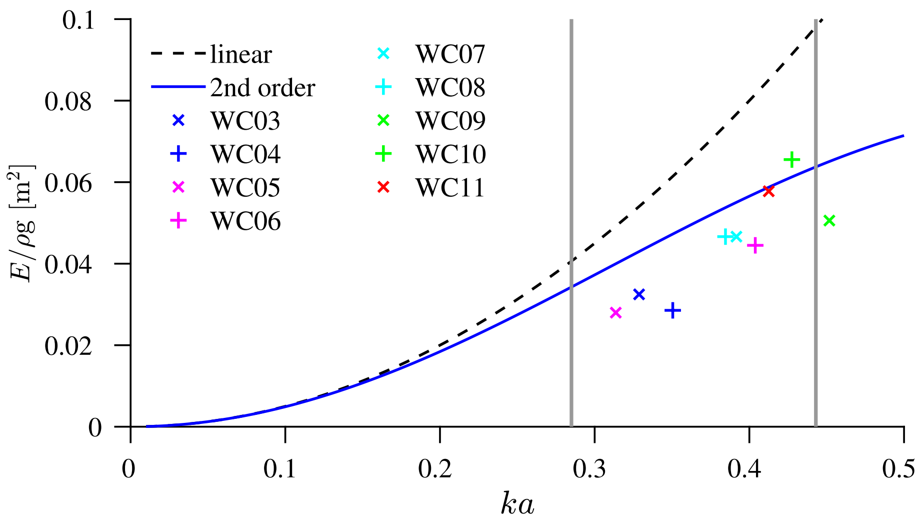

Fig. 3. Standing wave energy estimated using linear and second order wave theory. The laboratory tests are indicated by markers.

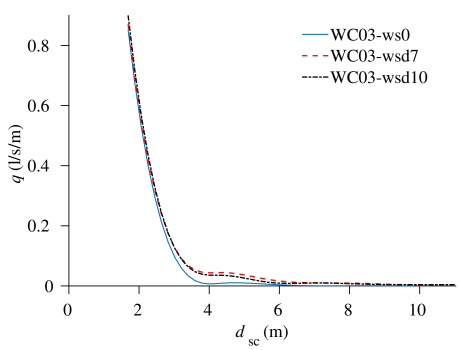

(a)

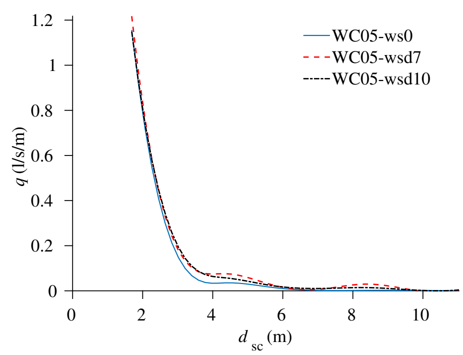

(b)

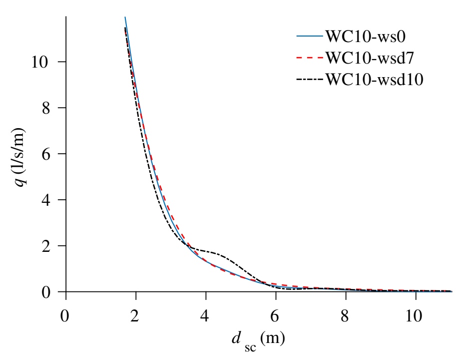

(c)

Fig. 4. Overtopping rates measured per unit sea defence crest width for Type A overtopping: ws0, wsd7 and wsd10 refer to three different wind speeds, namely zero; wind speed dial 7 (1.4m/s) and wind speed dial 10 (1.7m/s) for (a)WC03; (b) WC05 and (c) WC10.

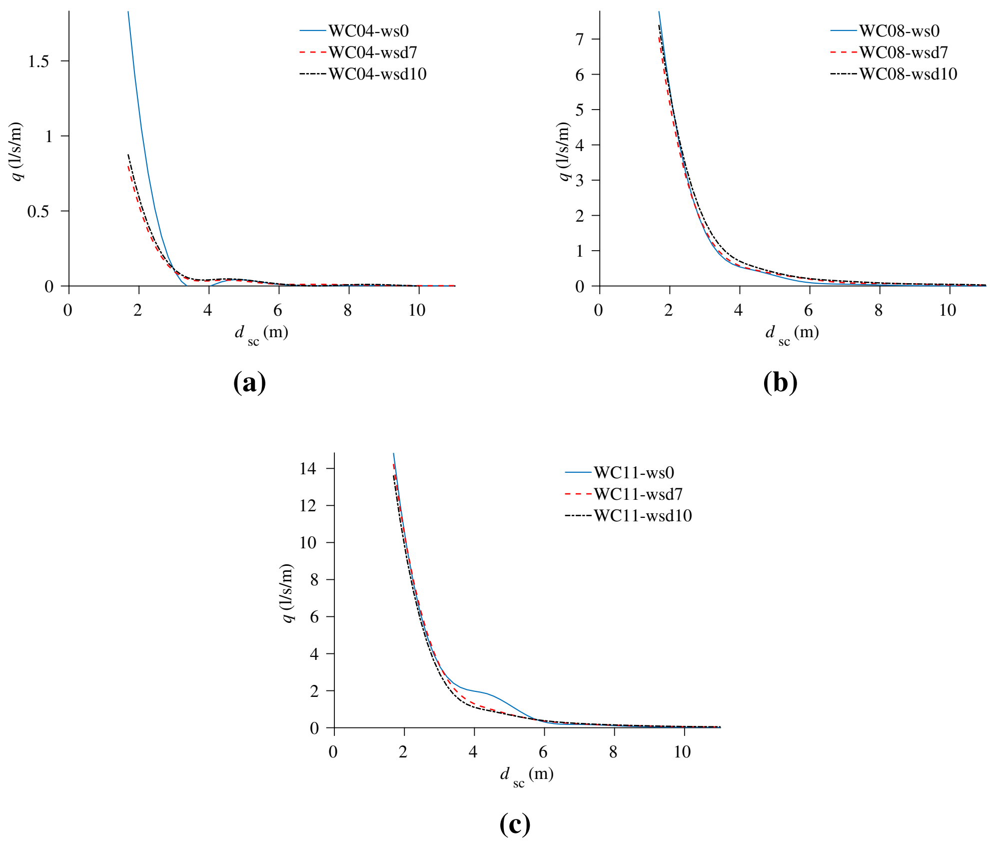

Fig. 5. Overtopping rates measured per unit sea defence crest width for Type B overtopping: ws0, wsd7 and wsd10 refer to three different wind speeds, namely zero; wind speed dial 7 (1.4m/s) and wind speed dial 10 (1.7m/s) for (a)WC04; (b) WC08 and (c) WC11.

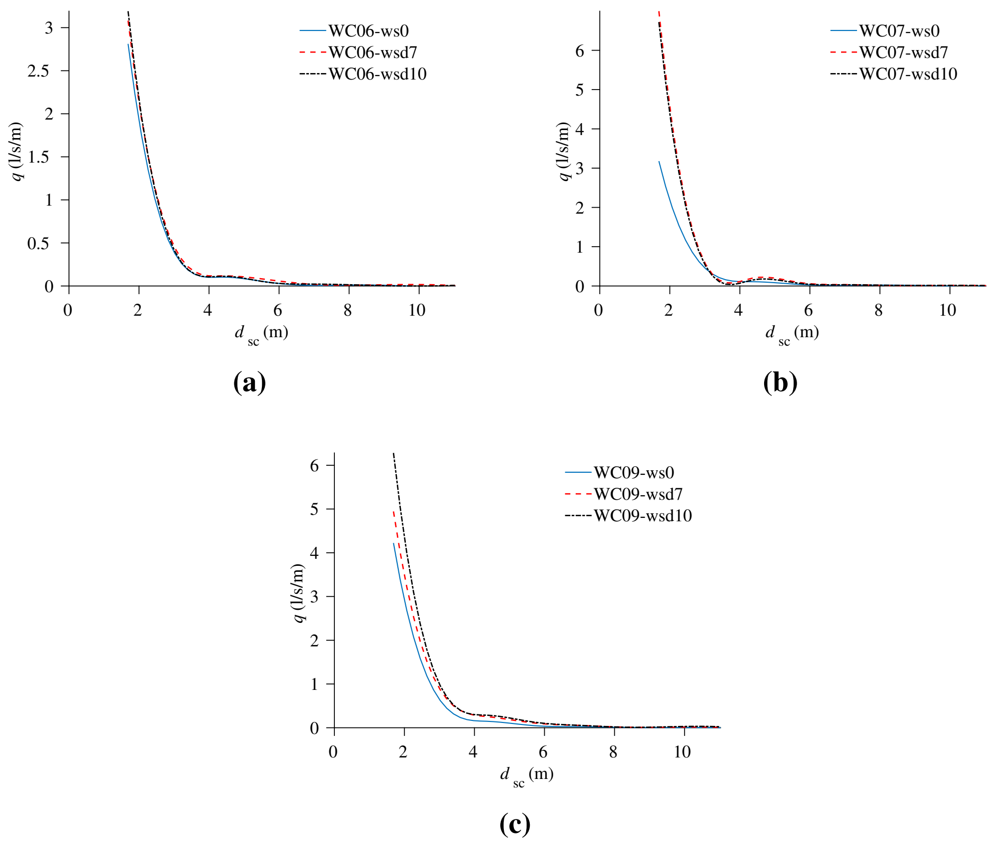

Fig. 6. Overtopping rates measured per unit sea defence crest width for Type C overtopping: ws0, wsd7 and wsd10 refer to three different wind speeds, namely zero; wind speed dial 7 (1.4m/s) and wind speed dial 10 (1.7m/s) for (a)WC06; (b) WC07 and (c) WC09.

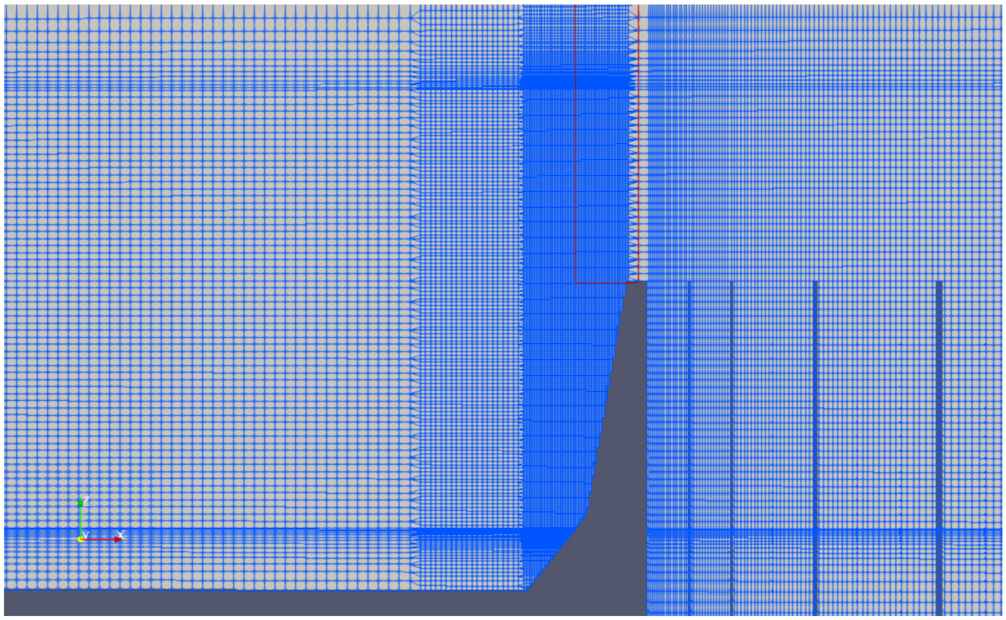

Fig. 7. Zoomed view of the mesh structure adopted near the sea defence model in the CFD computations. The outline in red is the wind zone to provide the desired wind speed. The direction of the incident wave is from left to right.

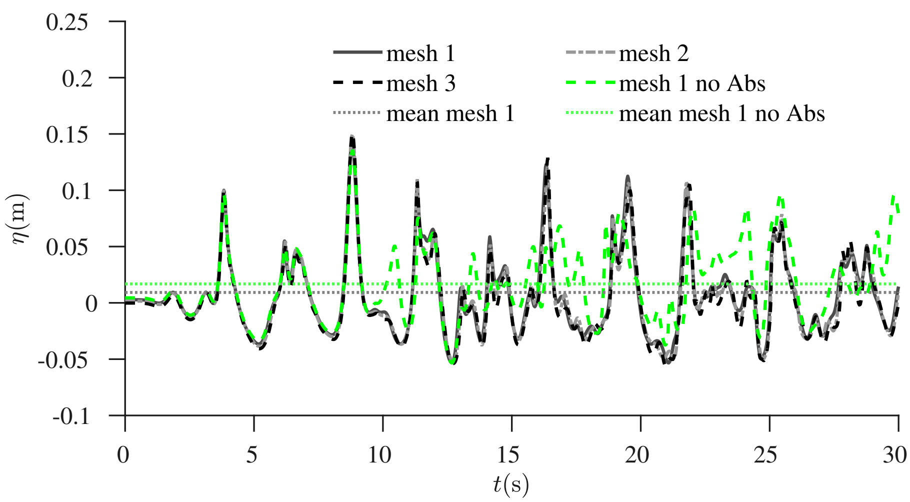

Fig. 8. Free surface elevations measured at 1.2m from the inlet of the computational domain in three different meshes and without active wave absorption all subjected to WC09.

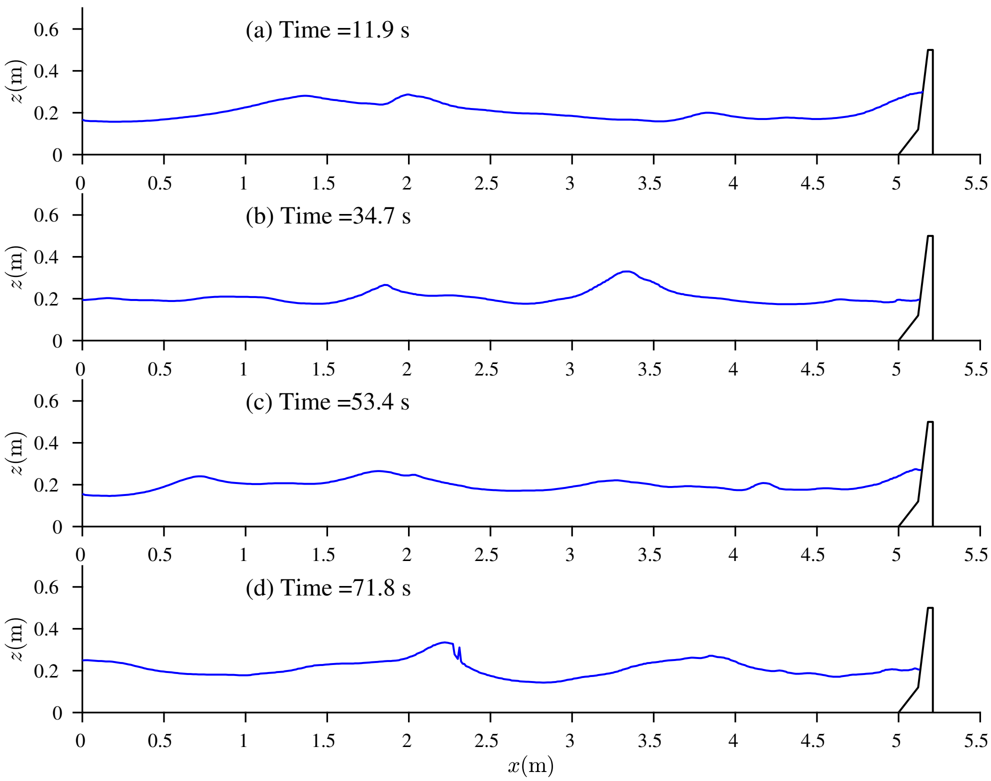

Fig. 9. Numerical simulation of waves under wave condition WC09 in OpenFOAM at various instants of time: (a) at t = 11.9s; (b) at t = 34.7s; (c) at t = 53.4s and (d) at t = 71.8s.

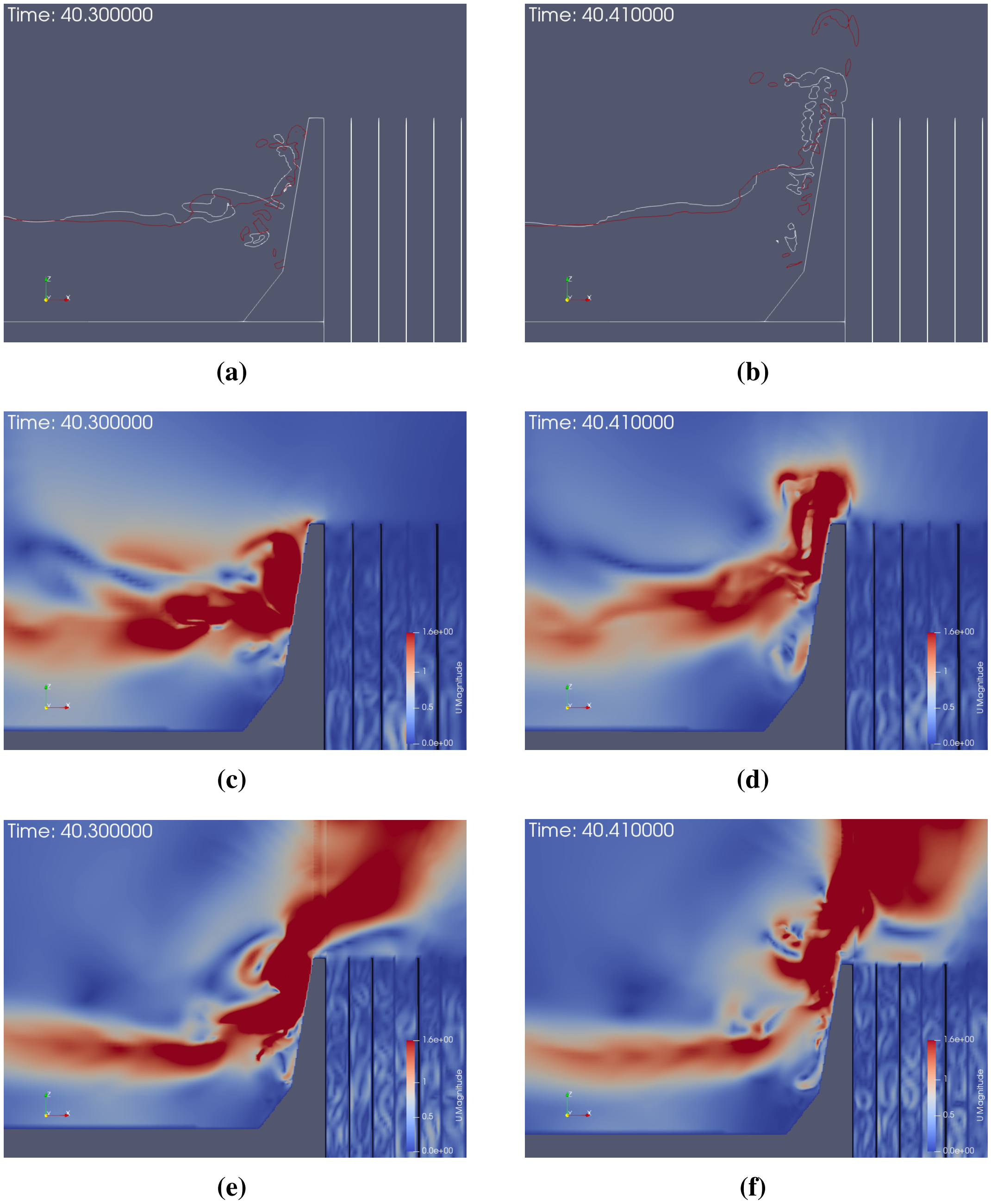

Fig. 10. Comparison of the wave profiles and velocity fields in various time instants during the wave impact on the sea defence during an overtopping cycle in Type A: (a) and (b) the free surface in white is from simulations with no wind action and the free surface in red is from the wind speed 1.55 m/s; (c) and (d) the velocity fields without wind; (e) and (f) the velocity fields with wind impact. The vertical and the horizontal extends are both of around 1m.

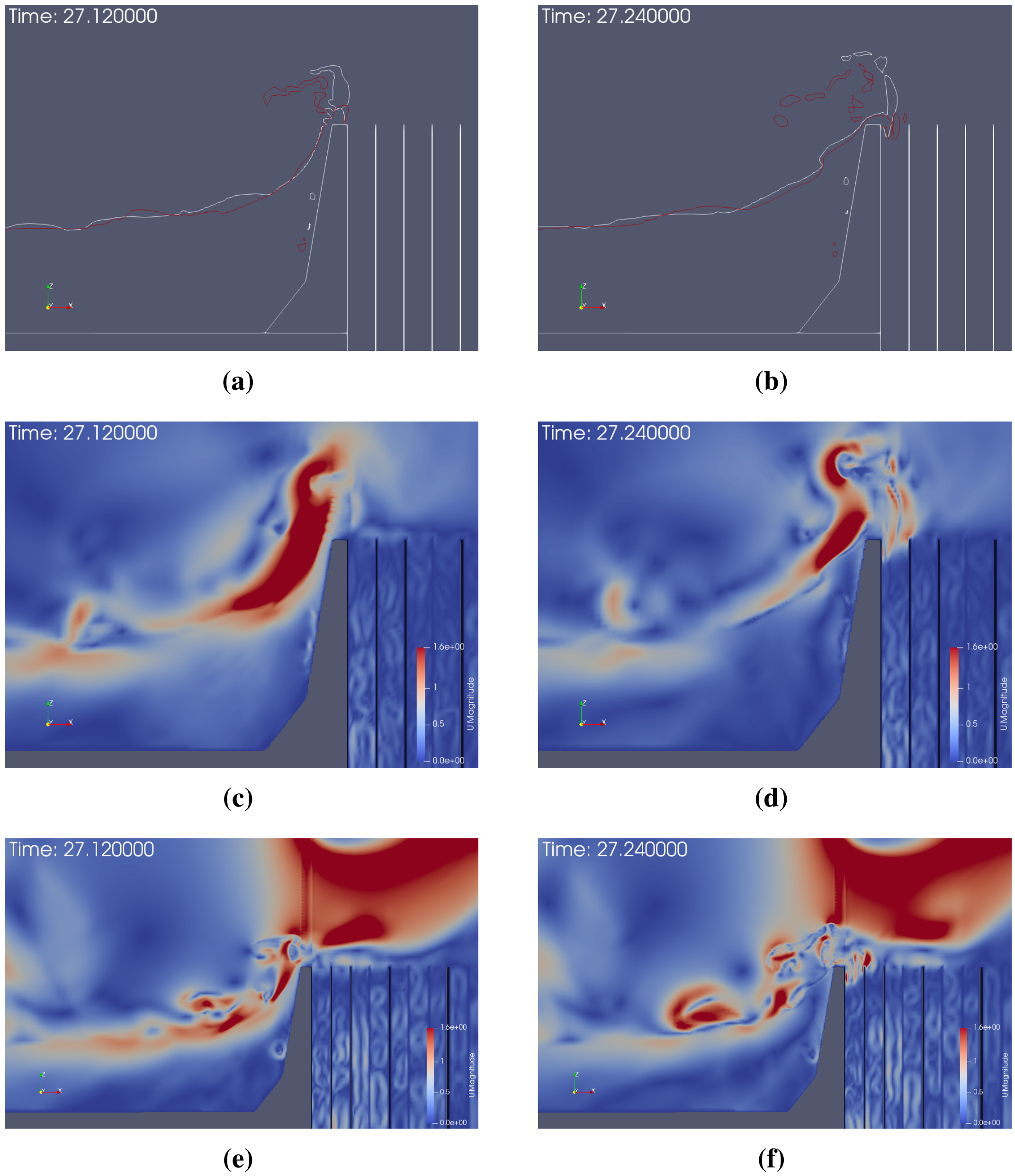

Fig. 11. Comparison of the wave profiles and velocity fields in various time instants during the wave impact on the sea defence during an overtopping cycle in Type B: (a) and (b) the free surface in white is from simulations with no wind action and the free surface in red is from the wind speed 1.55 m/s; (c) and (d) the velocity fields without wind; (e) and (f) the velocity fields with wind impact. The vertical and the horizontal extends are both of around 1m.

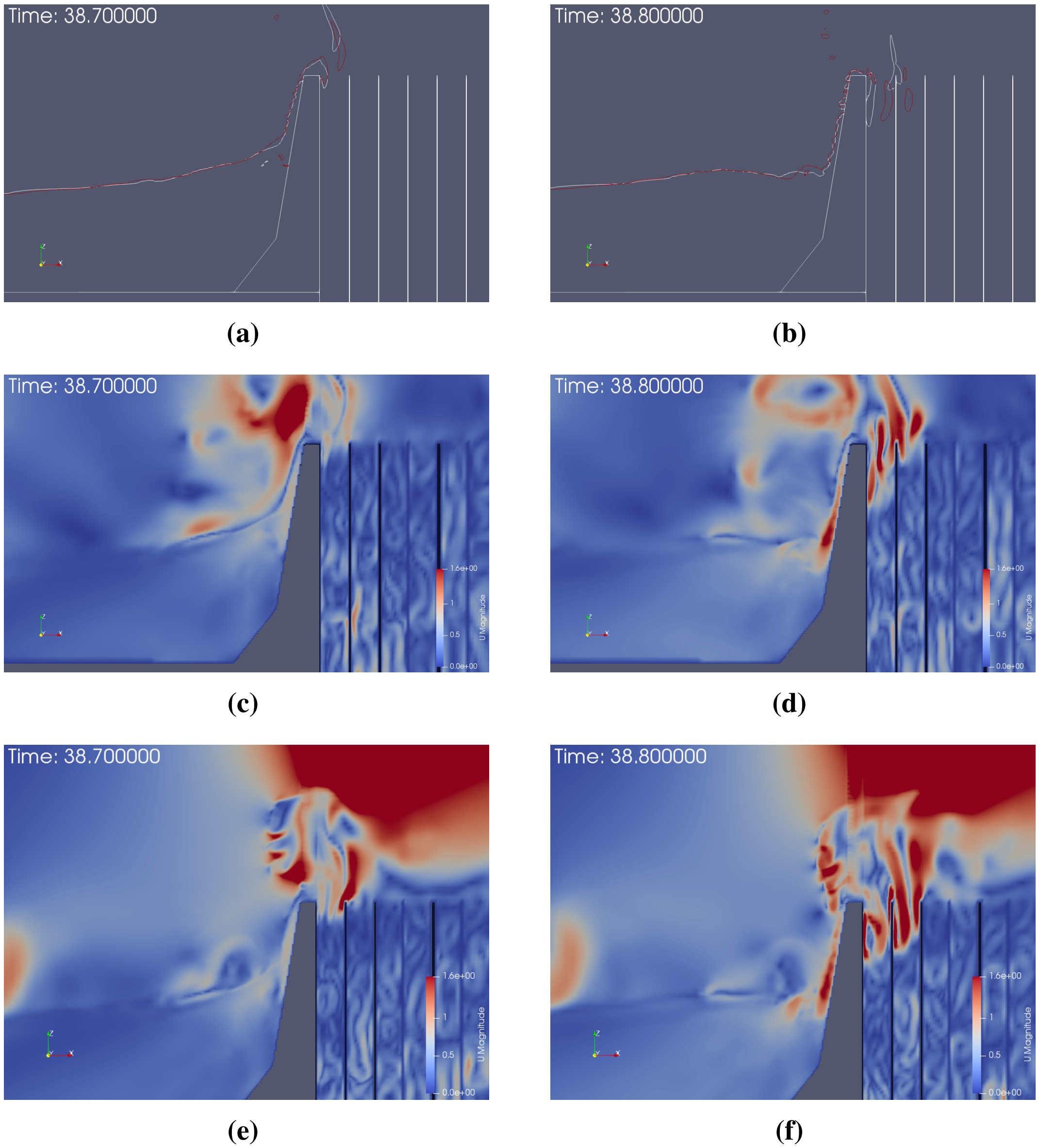

Fig. 12. Comparison of the wave profiles and velocity fields in various time instants during the wave impact on the sea defence during an overtopping cycle in Type C: (a) and (b) the free surface in white is from simulations with no wind action and the free surface in red is from the wind speed 1.55 m/s; (c) and (d) the velocity fields without wind; (e) and (f) the velocity fields with wind impact. The vertical and the horizontal extends are both of around 1m.

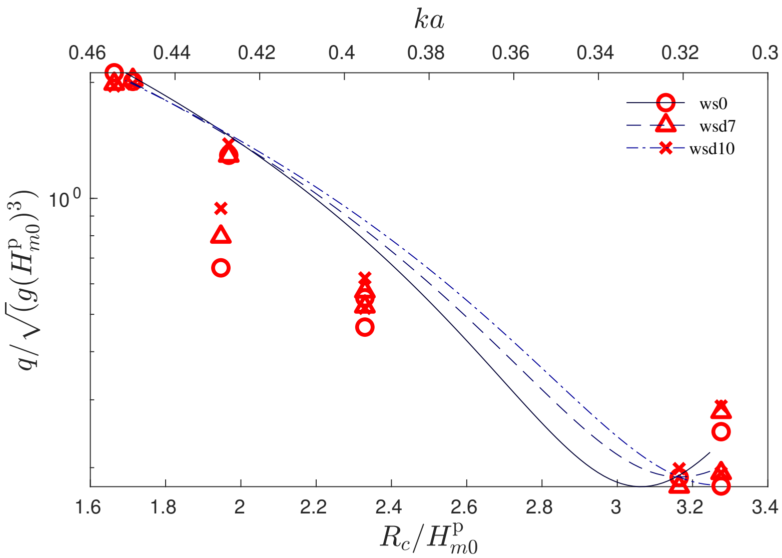

Fig. 13. Overtopping rates over normalized free board (bottom x-axis label) and wave steepness (upper x-axis label).

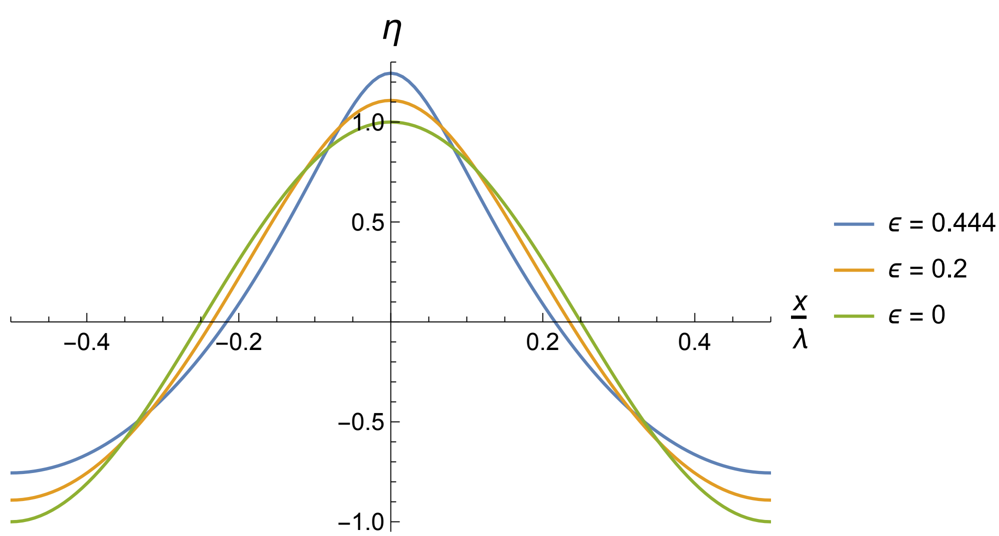

Fig. 14. Shape of standing wave of different steepness $\epsilon = Hk/2$. Here H is the wave height, k is the wavenumber, and λ is the wavelength. The limiting steepness was assumed according to the Stokes theory as $\epsilon_{max} = 0.444$.